Electronic Supplementary Information

Enhancing Thermoelectric Performance of SnSe$_{1-x}$Te$_x$ Nanoplates through Band Engineering

Min Hong[a], Zhi-Gang Chen[*,b,a], Lei Yang[a], Thomas C. Chasapis[c,d], Stephen Dongmin Kang[d], Yichao Zou[a], Graeme John Auchterlonie[e], Mercouri G. Kanatzidis[c], G. Jeffrey Snyder[d], and Jin Zou[*,a,e]

[a]Materials Engineering, University of Queensland, Brisbane, Queensland 4072, Australia

[b]Centre of Future Materials, University of Southern Queensland, Springfield, Queensland 4300, Australia

[c]Department of Chemistry, Northwestern University, Evanston, Illinois 60208, USA

[d]Department of Materials Science and Engineering, Northwestern University, Evanston, Illinois 60208, USA

[e] Centre for Microscopy and Microanalysis, University of Queensland, Brisbane, Queensland 4072, Australia

[*]Address correspondence to

j.zou@uq.edu.au

zhigang.chen@usq.edu.au

1. Determination of lattice parameters

The lattice spacing of the atomic planes (d_{hkl}) and its lattice parameters (a, b and c) for orthorhombic structure can be calculated by[1]

$$\frac{1}{d_{hkl}^2} = \frac{h^2}{a^2} + \frac{k^2}{b^2} + \frac{l^2}{c^2} \qquad （S1）$$

where *hkl* are the index of the {*hkl*} atomic planes. Since d_{hkl} can be measured from XRD patterns, *a*, *c*, and *b* can be respectively determined by using the 400*, 201*, and 511* peaks in their 2θ for each kind of nanoplates with different $SnSe_{1-x}Te_x$ concentration, as presented in Fig. S1. Then, the volume of the unit cell can be determined by[1]

$$V = abc \qquad （S2）$$
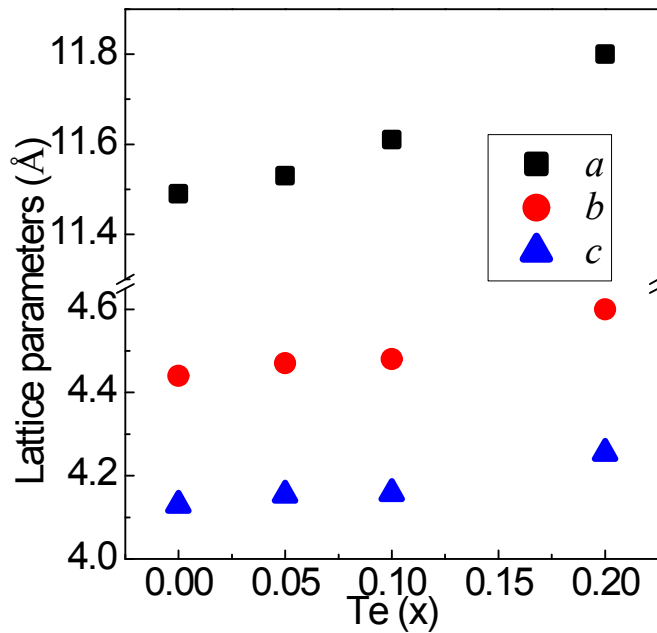

Fig. S1 Determined lattice parameters for different $SnSe_{1-x}Te_x$ nanoplates.

2. Orientation factor of sintered pellets

The orientation factor of the (x00) planes (f) was estimated from the XRD patterns by the Lotgering method,[2] $f=(P-P_0)/1-P_0$, where $P=\Sigma I(001)/\Sigma I(h\ k\ l)$ and $P_0=\Sigma I^0(001)/\Sigma I^0(h\ k\ l)$ with $I(h\ k\ l)$ and $I^0(h\ k\ l)$ denoting the intensities of ($h\ k\ l$) peaks for sintered and the standard SnSe (JCPDS No. 48-1224), respectively.

Table S1 Orientation factor of sintered pellets along in-plane and out-of-plane direction

f for (x00) planes	SnSe	SnSe$_{0.95}$Te$_{0.05}$	SnSe$_{0.95}$Te$_{0.1}$	SnSe$_{0.95}$Te$_{0.2}$
In-plane	0.415	0.420	0.418	0.423
Out-of-plane	0.017	0.012	0.016	0.010

3. Equations for modeling studies

Thermoelectric properties of single parabolic band model are given by[3,4]

Seebeck coefficient

$$S = \frac{k_B}{e}\left[\frac{2F_1(\eta)}{F_0(\eta)} - \eta\right], \tag{S3}$$

Hall carrier concentration

$$n_H = \frac{\left(2m_d^* k_B T\right)^{\frac{3}{2}}}{3\pi^2 \hbar^3}\frac{F_{1/2}(\eta)}{A}, \tag{S4}$$

Hall carrier mobility

$$\mu_H = \mu_0 \frac{\sqrt{\pi}}{2}\frac{F_0(\eta)}{F_{1/2}(\eta)}, \tag{S5}$$

Hall factor

$$A = \frac{3}{4}\frac{F_{1/2}F_{-1/2}}{\left(F_0\right)^2}, \tag{S6}$$

Electrical conductivity

$$\sigma = n_H \mu_H e, \tag{S7}$$

Generalized Fermi integration

$$F_n(\eta) = \int_0^\infty \frac{\varepsilon^n}{1+\exp(\varepsilon-\eta)}d\varepsilon, \tag{S8}$$

Electrical thermal conductivity is calculated according to the Wiedemann–Franz law, namely

4

$$\kappa_e = L\sigma T \, , \qquad \qquad (S9)$$

with L representing the Lorenz number, and give by

$$L = \left(\frac{k_B}{e}\right)^2 \left[\frac{3F_2(\eta)}{F_0(\eta)} - \left(\frac{2F_2(\eta)}{F_0(\eta)}\right)^2\right] . \qquad \qquad (S10)$$

In the above equations, η is the reduced Fermi level, ε is the reduced energy, k_B is Boltzmann constant, and e is the elementary charge, respectively.[5,6]

In the case of three valance bands, the total thermoelectric properties are calculated using the following equations.[7,8]

Total electrical conductivity

$$\sigma_{tot} = \sigma_1 + \sigma_2 + \sigma_3 \, , \qquad \qquad (S11)$$

Total Seebeck coefficient

$$S_{tot} = \frac{S_1\sigma_1 + S_2\sigma_2 + S_3\sigma_3}{\sigma_1 + \sigma_2 + \sigma_3} \, , \qquad \qquad (S12)$$

Total Lorenz number

$$L_{tot} = \frac{L_1\sigma_1 + L_2\sigma_2 + L_3\sigma_3}{\sigma_1 + \sigma_2 + \sigma_3} \, , \qquad \qquad (S13)$$

Total Hall coefficient

$$R_{H_{tot}} = \frac{R_{H_1}\sigma_1^2 + R_{H_2}\sigma_2^2 + R_{H_3}\sigma_3^2}{(\sigma_1 + \sigma_2 + \sigma_3)^2} \, , \qquad \qquad (S14)$$

Total Hall carrier concentration

$$n_{H_{tot}} = \frac{1}{eR_{H_{tot}}} \; , \tag{S15}$$

Total Hall carrier mobility

$$\mu_{H_{tot}} = \sigma_{tot} R_{H_{tot}} \; . \tag{S16}$$

In above equations, subscripts of 1, 2, and 3 correspond to tensors contributed by the VB_1, VB_2, and VB_3, respectively.

The analysis was first performed on the assumption of two interacting valance bands, $i.e.$ VB_1 and VB_2. For x = 0, a good fit to the experimental data was obtained for mobility ratios μ_{oVB1} / μ_{oVB2} in the range 1.8 to 2.2 and band offsets $VB_1 - VB_2$ in the range 35 − 40 meV. Then, the two-band model was extended to higher x values. Due to the large number of unknown parameters involved during the calculation, we assumed that the partial mobilities remain unchanged upon alloying with a constant mobility ratio around 2. The application of the two-band model for x = 0.05 and x = 0.1 compositions yielded acceptable fits upon an almost linear reduction of the valence band offset VB_1-VB_2. However, for x = 0.2 the two-band model $S^2\sigma$ and μ_H were found to deviate significantly from the experimental values, regardless of the two-band model parameters, $i.e.$ the mobility ratio and the band offset. The fit was significantly improved by the incorporation of the third valence band VB_3. For the offset VB_1-VB_2, we used the value obtained from the linear extrapolation of the best fit values calculated for x = 0, 0.05 and 0.1. Then the mobility of the third band and the band offset VB_1-VB_3 were adjusted in order to fit the experimental power factor and the Hall mobility of the x = 0.2 material. A final refinement was achieved after applying the three-band model to all x values. The comparison of the experimental data with the best fit calculated lines is summarized in Fig.s S5-S8. Focusing on the power factor results, the two-band model provides good quality fits for the x = 0, 0.05 and 0.1, but for x = 0.2 the model deviates strongly. We should note that while these values yielded acceptable fits they are not unique. In other words, other sets of parameters may provide adequate fits. Our procedure provides a quantitative example that a multi-band

description can adequately reflect the room temperature compositional dependence of the transport coefficients.

4. Examination of anisotropic behavior of thermoelectric properties

To examine the anisotropy behavior, we measured the thermoelectric properties of $SnSe_{0.9}Te_{0.1}$ pellet as an example. Fig. S2 shows the obtained S, σ, $S^2\sigma$, κ, and zT as a function of T along both in-plane and out-of-plane directions.
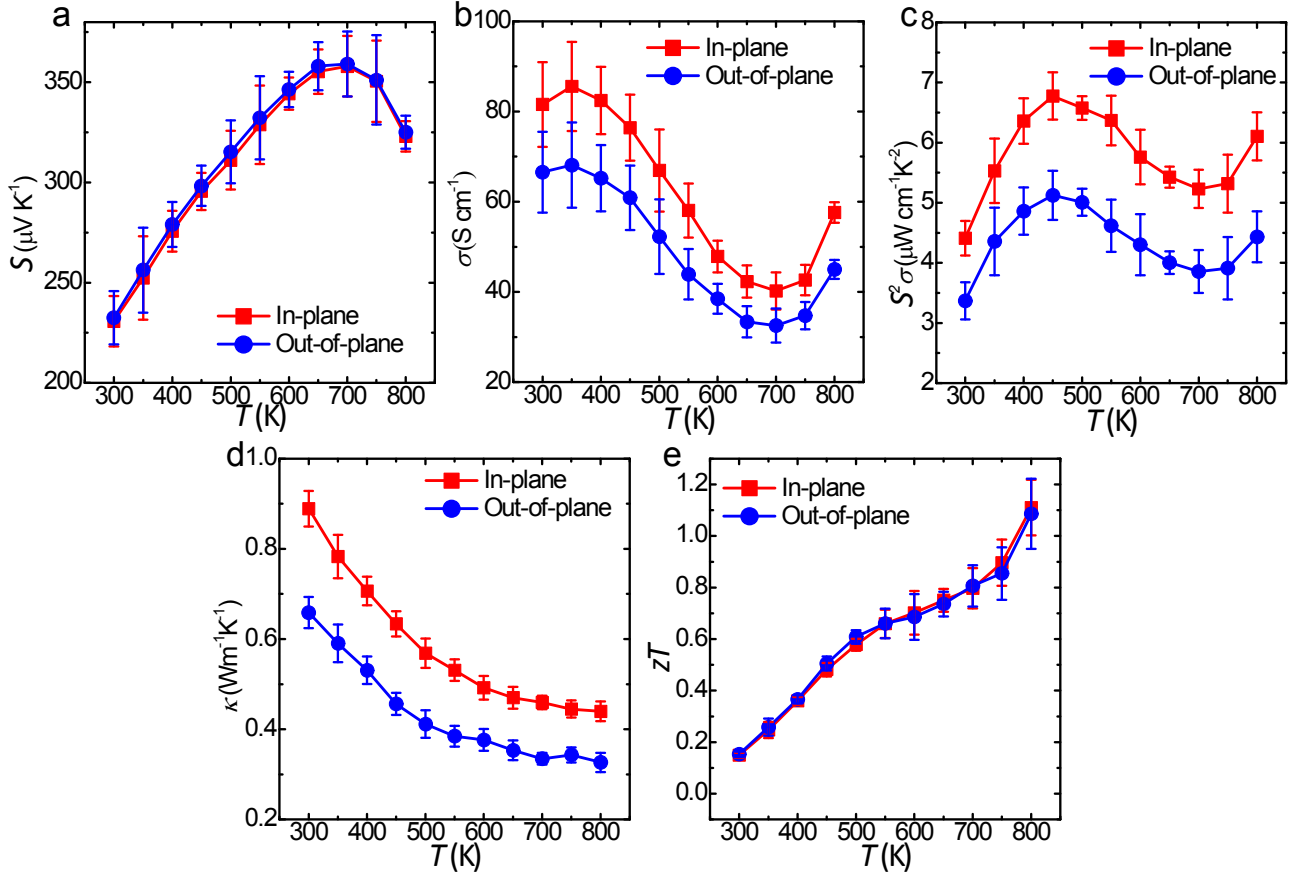

Fig. S2 The in-plan and out-of-plan thermoelectric properties of $SnSeTe_{0.1}$: (a) S, (b) σ, (c) $S^2\sigma$ (d) κ, and (e) zT, respectively.

5. Determined Lorenz number (L)

To calculate L, we firstly calculated η using measured S based on Equation (S3). Through substituting calculated η into Equation (S10), we calculated L for different $SnSe_{1-x}Te_x$. Fig. S3 shows the obtained L for different $SnSe_{1-x}Te_x$.
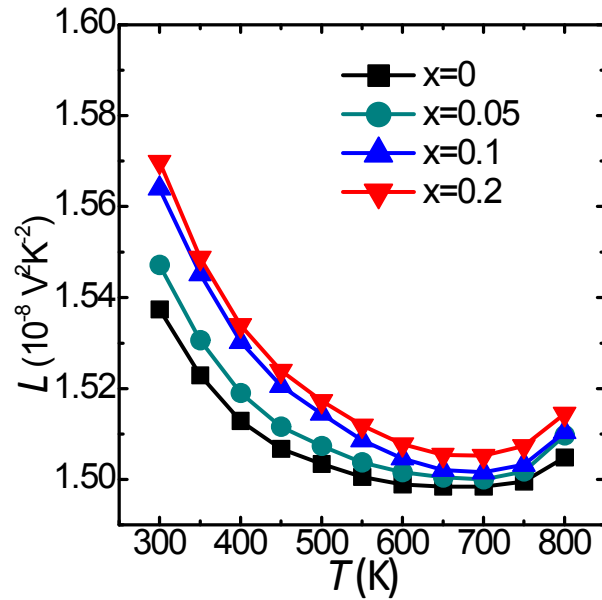
Fig. S3 Determined L for $SnSe_{1-x}Te_x$ as a function of temperature.

6. Examination of the thermal stability for obtained thermoelectric properties

To evaluate the stability of thermoelectric properties in our pellets, we tested the $SnSe_{0.9}Te_{0.1}$ pellet (as a representative example) for three heating-cooling cycles. Fig. S4 shows the obtained S, σ, $S^2\sigma$ κ, and zT as a function of T.
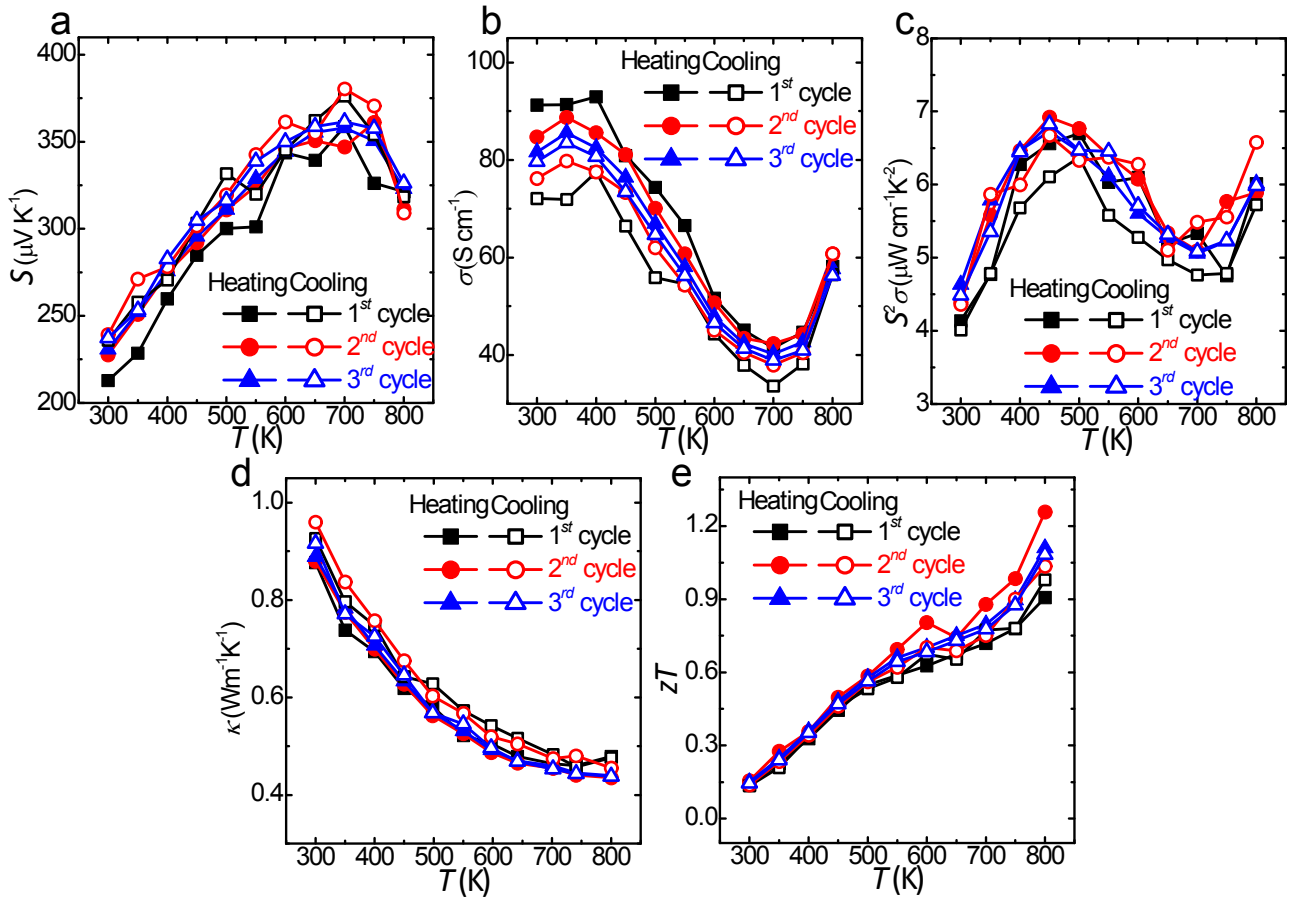
Fig. S4 Measured thermoelectric properties of sintered $SnSe_{0.9}Te_{0.1}$ pellet for three heating-cooling cycles: (a) S, (b) σ, (c) $S^2\sigma$ (d) κ, and (e) zT, respectively.

7. Hall measurement and EPMA results

To analyze the measured electronic transport properties, we measured T-dependent n_H and μ_H for $SnSe_{1-x}Te_x$ over $300 - 700$ K, shown in Fig. S5. To examine the variation of compositions in our $SnSe_{1-x}Te_x$, we applied EPMA to determine the elemental ratios, shown in Table S1.
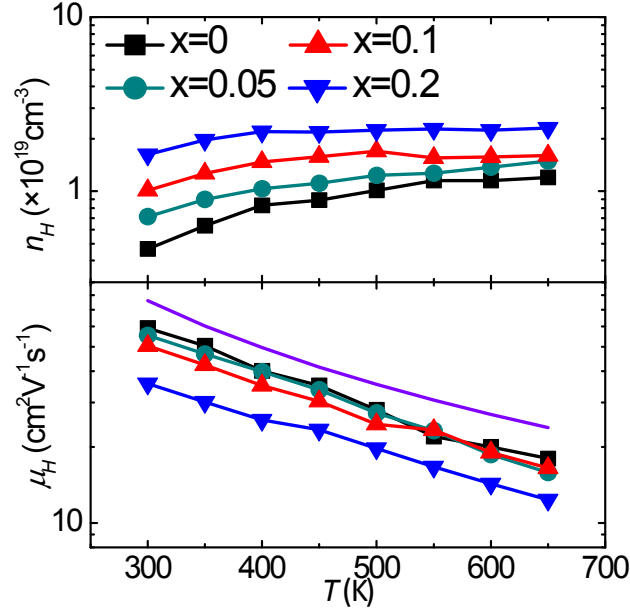

Fig. S5 Temperature-dependent n_H and μ_H for $SnSe_{1-x}Te_x$.

Table S2 The determined compositions of sintered $SnSe_{1-x}Te_x$ pellets by EPMA.

Samples	Te (mol %)	Se (mol %)	Sn (mol %)
SnSe	0	50.418	49.581
$SnSe_{0.95}Te_{0.05}$	4.268	46.241	49.491
$SnSe_{0.9}Te_{0.1}$	11.801	38.847	49.352
$SnSe_{0.8}Te_{0.2}$	18.137	32.721	49.141

8. Modelling studies

To understand the enhanced $S^2\sigma$, we applied the three-band model to analyze the obtained electronic transport coefficients. From which, we determined the energy offsets of $VB_1 - VB_2$ and $VB_1 - VB_3$ for our $SnSe_{1-x}Te_x$ pellets. Fig. S6a shows these offsets. Fig. S6b shows the positions of VB_1, VB_2, and VB_3. Based on the determined energy offsets, we applied the three-band model to fit our obtained electronic transport coefficients. Fig. S7 $-$ S10 show the calculated S and μ_H as a function of n_H, and $S^2\sigma$ as a function of σ for $SnSe_{1-x}Te_x$ with x = 0, 0.05, 0.1, and 0.2, respectively.
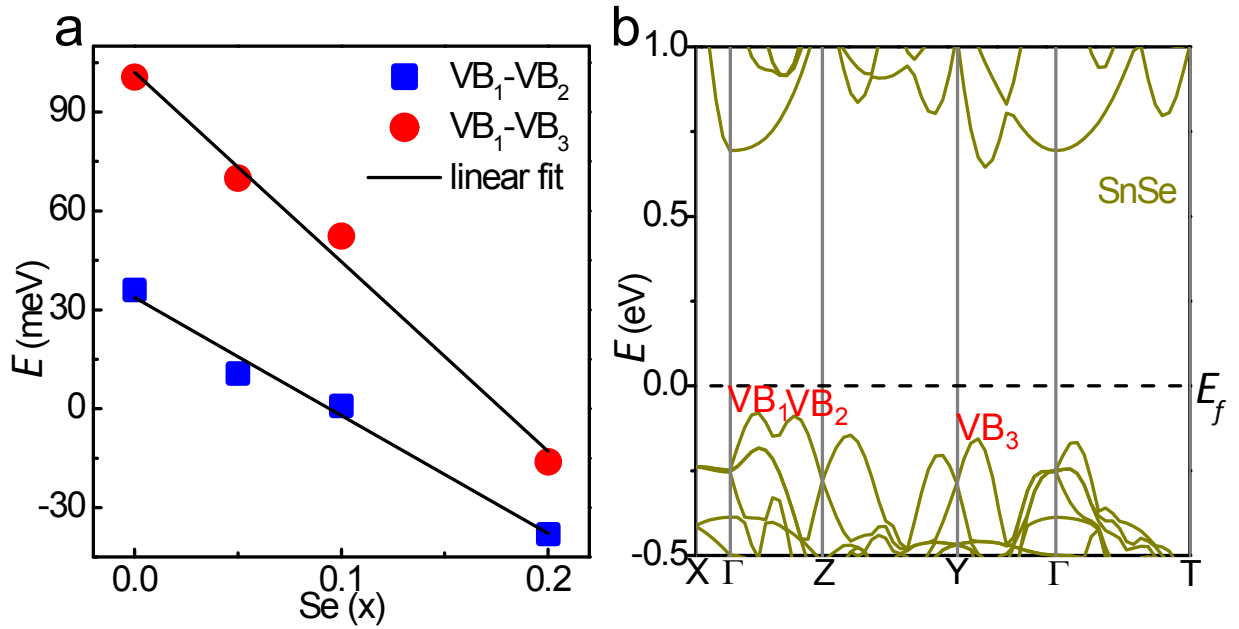
Fig. S6 (a) Determined energy offset of $VB_1 - VB_2$, and $VB_1 - VB_3$ from multiband model analysis of the room temperature transport properties. (b) The band structure of SnSe as an example to demonstrate positions of VB_1, VB_2, and VB_3.
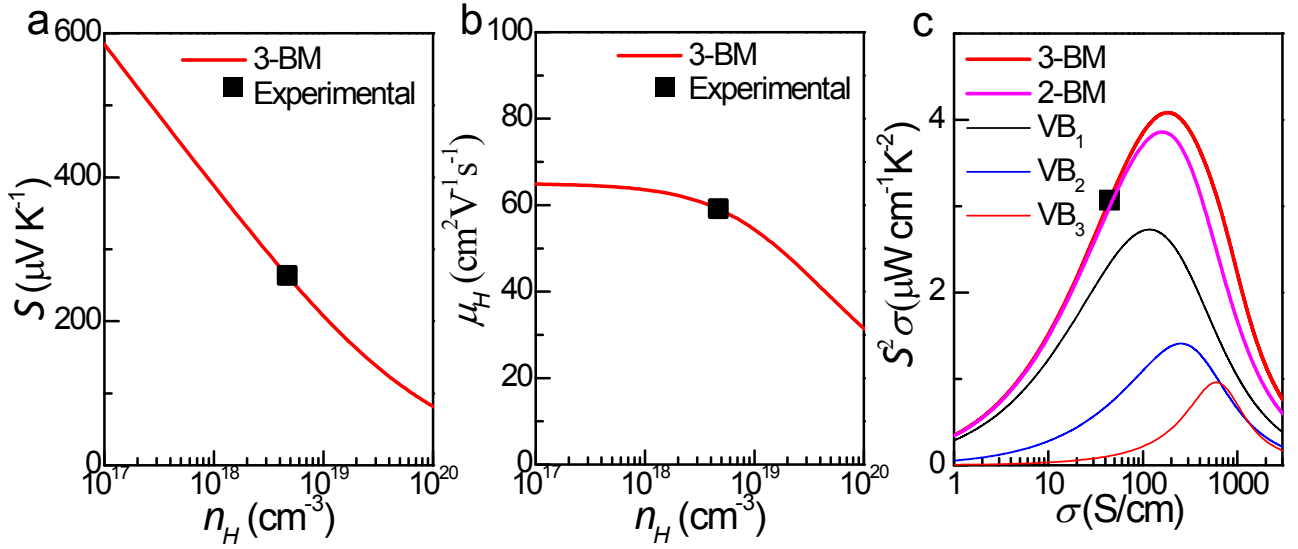
Fig. S7 (a) (b) Calculated curves of S and μ_H as a function of n_H using the three-band model, and (c) calculated curve of $S^2\sigma$ as a function of σ for SnSe using different models compared with the corresponding data points at 300 K.
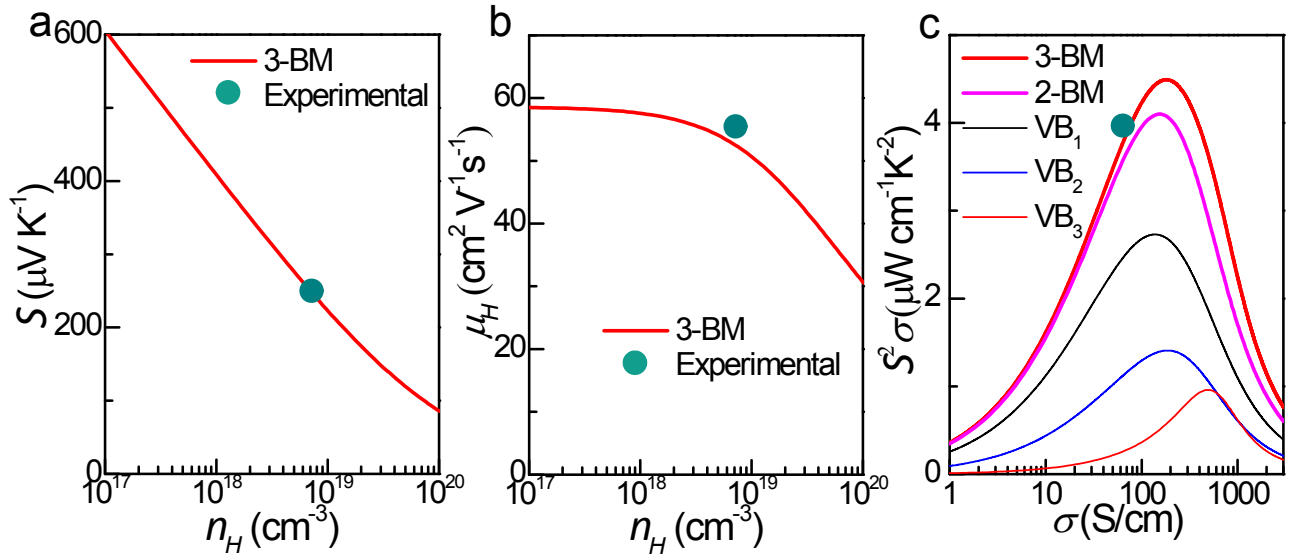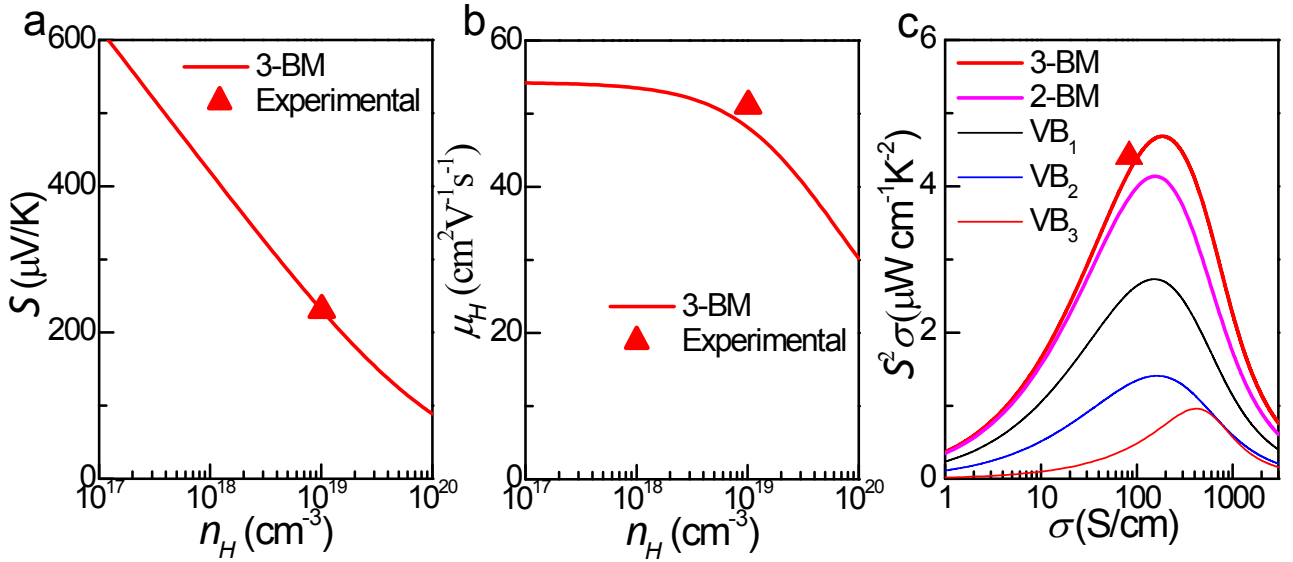

Fig. S8 (a) (b) Calculated curves of S and μ_H as a function of n_H using the three-band model, and (c) calculated curve of $S^2\sigma$ as a function of σ for SnSe$_{0.95}$Te$_{0.05}$ using different models compared with the corresponding data points at 300 K.
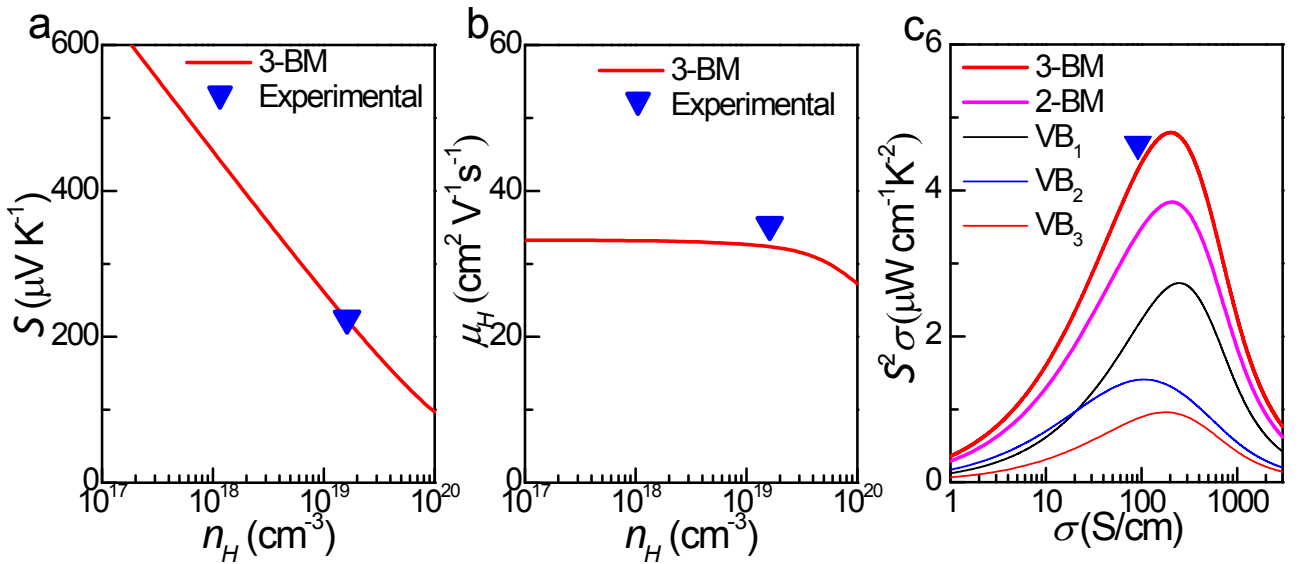
Fig. S9 (a) (b) Calculated curves of S and μ_H as a function of n_H using the three-band model, and (c) calculated curve of $S^2\sigma$ as a function of σ for $SnSe_{0.9}Te_{0.1}$ using different models compared with the corresponding data points at 300 K.

Fig. S10 (a) (b) Calculated curves of S and μ_H as a function of n_H using the three-band bands model, and (c) calculated curve of $S^2\sigma$ as a function of σ for $SnSe_{0.8}Te_{0.2}$ using different models compared with the corresponding data points at 300 K.

9. Determination of optical band gaps

In order to fully interpret our optical data, we used the Tauc-model [9], and linearly fitted the normalized absorption spectrum in the indirect (*i.e.* $(\alpha/s)^{1/2}$ against photon energy $\hbar\omega$ with $\hbar$ and ω representing the reduced Planck constant and phonon frequency) and the direct (*i.e.* $(\alpha/s)^2$ against $\hbar\omega$) band gap configurations. Fig. S11 – S14 show the determination of direct and indirect $E_{g,opt}$ for SnSe$_{1-x}$Te$_x$ with x = 0, 0.05, 0.1, and 0.2, respectively.
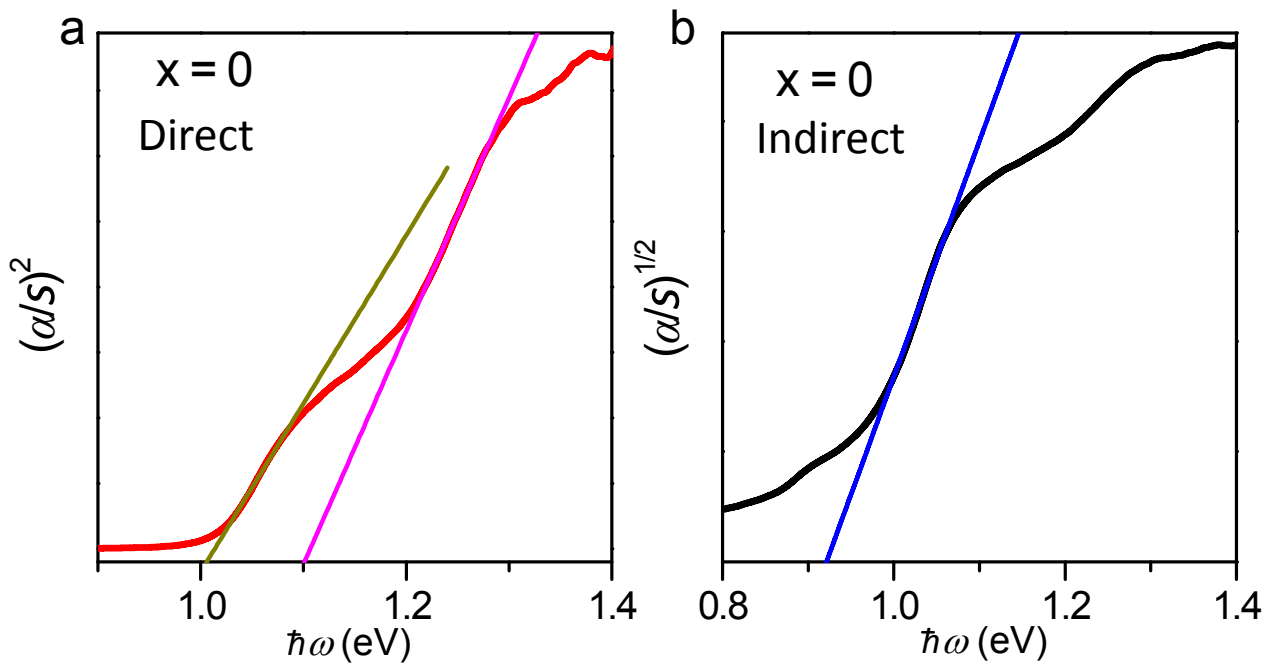

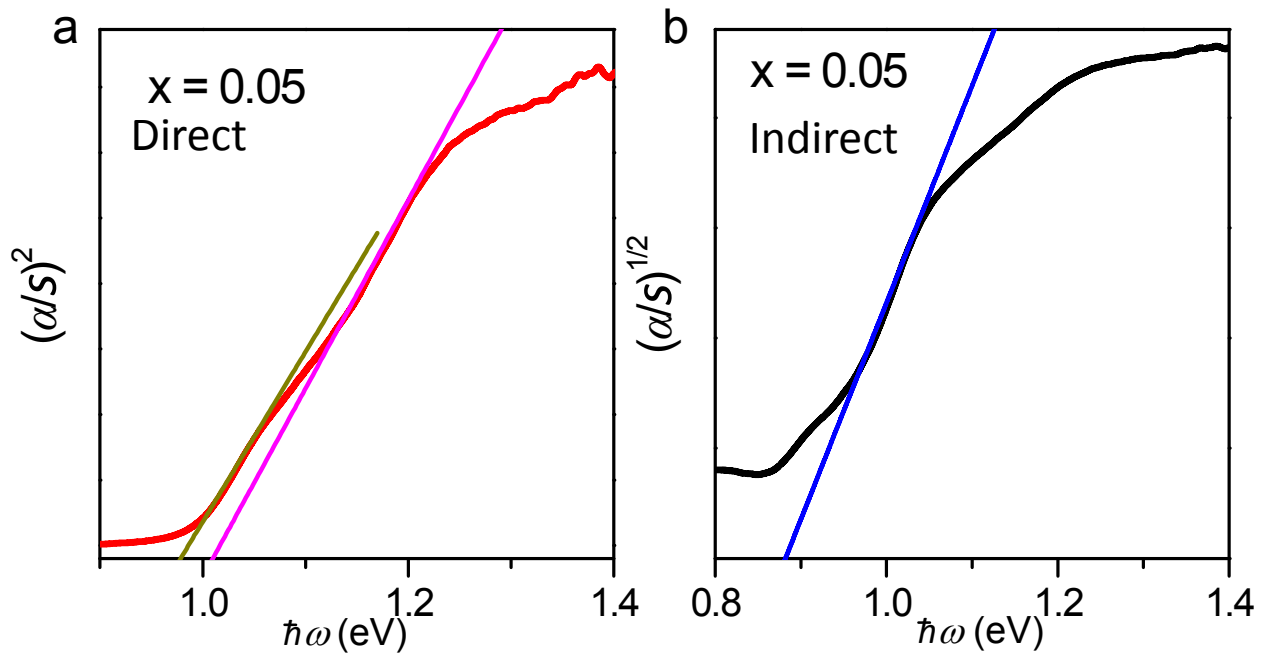Fig. S11 The determination of optical band gaps for SnSe in the direct (a) and (b) configurations.

Fig. S12 The determination of optical band gaps for SnSe$_{0.95}$Te$_{0.05}$ in the direct (a) and (b) configurations.
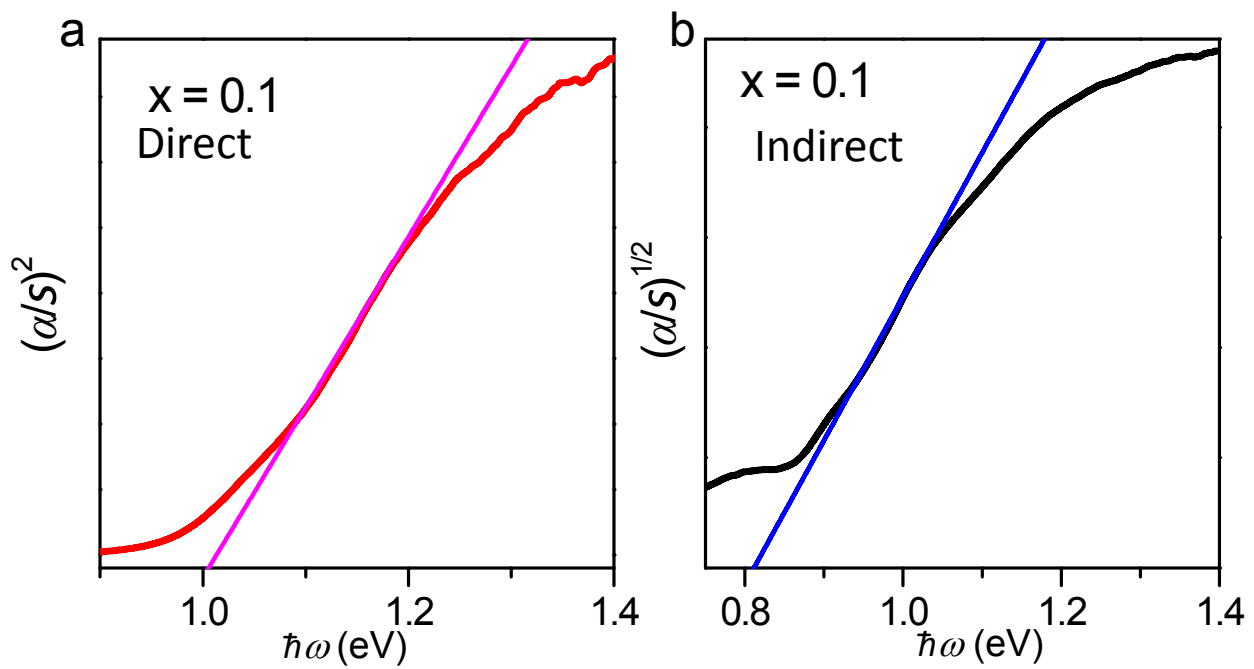

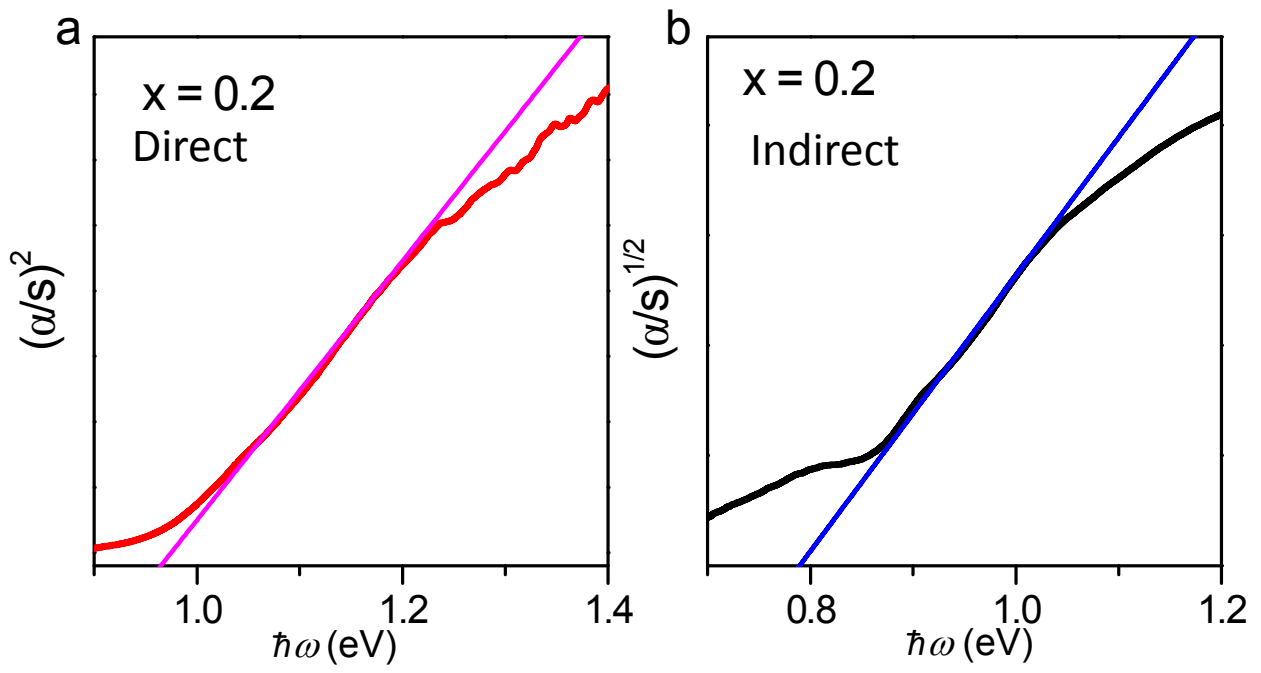Fig. S13 The determination of optical band gaps for SnSe$_{0.9}$Te$_{0.1}$ in the direct (a) and (b) configurations.

Fig. S14 The determination of optical band gaps for $SnSe_{0.8}Te_{0.2}$ in the direct (a) and (b) configurations.

References

1 Y. Waseda, E. Matsubara and K. Shinoda, *X-Ray Diffraction Crystallography*, Springer Press, Berlin, Heidelberg, 2011.

2 F. K. Lotgering, *J. Inorg. Nucl. Chem.*, 1959, **9**, 113-123.

3 C. L. Chen, H. Wang, Y. Y. Chen, T. Day and G. J. Snyder, *J. Mater. Chem. A*, 2014, **2**, 11171-11176.

4 Z. M. Gibbs, H.-S. Kim, H. Wang and G. J. Snyder, *Appl. Phys. Lett.*, 2015, **106**, 022112.

5 Y. Pei, Z. M. Gibbs, B. Balke, W. G. Zeier and G. J. Snyder, *Adv. Energy Mater.*, 2014, **4**, 1400486.

6 W. Liu, K. C. Lukas, K. McEnaney, S. Lee, Q. Zhang, C. P. Opeil, G. Chen and Z. Ren, *Energy Environ. Sci.*, 2013, **6**, 552-560.

7 M. Hong, Z.-G. Chen, Y. Pei, L. Yang and J. Zou, *Phys. Rev. B*, 2016, **94**, 161201.

8 L. Zhang, P. Xiao, L. Shi, G. Henkelman, J. B. Goodenough and J. Zhou, *J. Appl. Phys.*, 2015, **117**, 155103.

9 G. K. M. Thutupalli and S. G. Tomlin, *J. Phys. C*, 1977, **10**, 467-477.